JACS
JOURNAL OF THE AMERICAN CHEMICAL SOCIETY
Article
pubs.acs.org/JACS

Supramolecular Packing Controls H_2 Photocatalysis in Chromophore Amphiphile Hydrogels

Adam S. Weingarten,[†,‡] Roman V. Kazantsev,[†,‡] Liam C. Palmer,[†,§] Daniel J. Fairfield,[∥] Andrew R. Koltonow,[∥] and Samuel I. Stupp*[,†,‡,§,∥,⊥,#]

[†]Department of Chemistry, Northwestern University, Evanston, Illinois 60208, United States
[‡]Argonne-Northwestern Solar Energy Research (ANSER) Center, Northwestern University, Evanston, Illinois 60208, United States
[§]Simpson Querrey Institute for BioNanotechnology, Northwestern University, Chicago, Illinois 60611, United States
[∥]Department of Materials Science and Engineering, Northwestern University, Evanston, Illinois 60208, United States
[⊥]Department of Medicine, Northwestern University, Chicago, Illinois 60611, United States
[#]Department of Biomedical Engineering, Northwestern University, Evanston, Illinois 60208, United States

Supporting Information

ABSTRACT: Light harvesting supramolecular assemblies are potentially useful structures as components of solar-to-fuel conversion materials. The development of these functional constructs requires an understanding of optimal packing modes for chromophores. We investigated here assembly in water and the photocatalytic function of perylene monoimide chromophore amphiphiles with different alkyl linker lengths separating their hydrophobic core and the hydrophilic carboxylate headgroup. We found that these chromophore amphiphiles (CAs) self-assemble into charged nanostructures of increasing aspect ratio as the linker length is increased. The addition of salt to screen the charged nanostructures induced the formation of hydrogels and led to internal crystallization within some of the nanostructures. For linker lengths up to seven methylenes, the CAs were found to pack into 2D crystalline unit cells within ribbon-shaped nanostructures, whereas the nine methylene CAs assembled into long nanofibers without crystalline molecular packing. At the same time, the different molecular packing arrangements after charge screening led to different absorbance spectra, despite the identical electronic properties of all PMI amphiphiles. While the crystalline CAs formed electronically coupled H-aggregates, only CAs with intermediate linker lengths showed evidence of high intermolecular orbital overlap. Photocatalytic hydrogen production using a nickel-based catalyst was observed in all hydrogels, with the highest turnovers observed for CA gels having intermediate linker lengths. We conclude that the improved photocatalytic performance of the hydrogels formed by supramolecular assemblies of the intermediate linker CA molecules likely arises from improved exciton splitting efficiencies due to their higher orbital overlap.

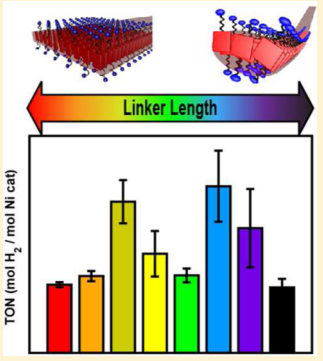

INTRODUCTION

The integration of light-harvesting nanostructures and fuel-producing catalysts is an interesting goal to develop materials with the capacity to generate solar fuels.[1] Natural photosynthetic systems have attained this integration by colocalizing light-harvesting arrays of π-conjugated chromophores with catalytic reaction centers.[2] While natural photosystems can be coupled to proton-reduction catalysts to efficiently convert sunlight directly into hydrogen (H_2),[3−5] synthetic materials are potentially better targets for renewable energy platforms. The ability of conjugated small molecules to engage in $\pi-\pi$ stacking has been utilized in solid-state photoconductors[6,7] and organic photovoltaic devices[8−11] to collect photogenerated charges at electrodes. Self-assembled gels could facilitate the light-driven water splitting reaction within a hydrated environment harboring chromophore−catalyst interactions.[12,13] A host of supramolecular, $\pi-\pi$ stacked materials have been reported,[14] with many studies finding that differences in molecular packing alter light harvesting or energy transport within supramolecular materials.[15−21]

We reported recently on photocatalysis using charged chromophore amphiphiles (CAs) containing perylene monoimide (PMI) moieties and carboxylate groups that assemble into ribbon-shaped nanostructures in water (see Scheme 1).[1] The choice of chromophore was based on PMI's high thermal, chemical, and acid stability as well as strong visible-light absorbance.[22] PMI derivatives have found use in covalent dyads[23,24] and small supramolecular assemblies[25,26] to promote electron−hole separation, a necessary mechanistic step for efficient fuel generation. Interestingly, we found that both gelation of aqueous solutions and internal crystallization within the nanoribbons occur simultaneously by simply adding monovalent, divalent, or polyvalent salts that screen repulsive electrostatic interactions. These CA hydrogels could photo-

Received: September 23, 2015
Published: November 21, 2015

DOI: 10.1021/jacs.5b10027
J. Am. Chem. Soc. 2015, 137, 15241−15246

Scheme 1. General Synthetic Procedure for the Preparation of Self-Assembling CAs with Varying Alkyl Linker Lengths

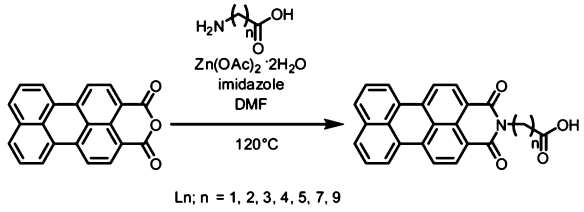

sensitize aqueous H_2 evolution in the presence of a water-soluble, cationic nickel proton reduction catalyst, visible light, and ascorbic acid as a source of electrons and protons.

The identification of advantageous packing arrangements to move energy to a catalyst is a crucial parameter for the development of efficient solar-to-fuel conversion supramolecular materials. In this work we have synthesized a series of seven CA molecules to probe the impact of molecular packing on photocatalytic hydrogen production. The structures of supramolecular assemblies formed by these molecules have also been characterized by electron microscopy, X-ray scattering, and UV−vis spectroscopy.

RESULTS AND DISCUSSION

The PMI derivatives studied here are designated as **L*n***, where *n* is the number of methylenes between the imide and the terminal carboxylic acid. These CAs were prepared by the condensation of perylene monoanhydride (PMA)[22] and commercially available or synthetically accessible[27] *ω*-amino-carboxylic acids (Scheme 1). Conversion of the carboxylic acid to the methyl ester vastly improved solubility of each molecule in organic solvents and enabled purification via recycling gel permeation chromatography (rGPC) (Figure S1). Once purified, we could regenerate the carboxylic acids using sulfuric acid to hydrolyze the ester.

We investigated the structure of CA assemblies in aqueous solution to determine how linker length variations altered nanostructure morphologies and molecular packing. The molecules in the homologous series are insoluble in water in their protonated form, but are soluble at least up to 11.5 mM concentrations with 1 equiv of NaOH. The CA assemblies formed by the water-soluble carboxylates were imaged using cryogenic transmission electron microscopy (cryo-TEM) to capture their solution-state morphologies (Figure 1a−g). **L1** and **L2** molecules assembled into ribbons hundreds of nanometers to micrometers in length (Figure 1a). In contrast, **L3** and **L4** formed small nanostructures of various widths that did not have a distinct morphology (Figure 1c, d, respectively). **L5** formed a mixture of thin and wide ribbons, while **L7** showed exclusively thin ribbons in water (Figure 1e, f, respectively). Lastly, microscopy of **L9** revealed micrometer-long nanostructures less than 10 nm in width (Figure 1g). The CA assembly morphologies clearly change by simply varying the linker length, with two dominant trends: increasing the linker length beyond one methylene reduces nanostructure dimensions, while increasing the linker length from five to nine methylenes results in increasing nanostructure aspect ratio.

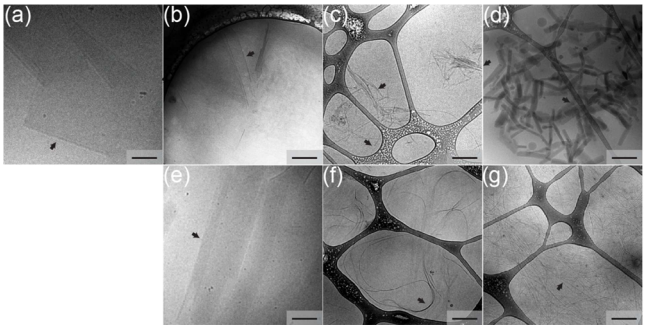

Figure 1. Cryo-TEM images of (a) **L1**, (b) **L2**, (c) **L3**, (d) **L4**, (e) **L5**, (f) **L7**, and (g) **L9** assemblies. Samples were prepared from 11.5 mM aqueous CA solutions. Scale bars are 300 nm.

We obtained small-angle X-ray scattering (SAXS) on bulk solutions of CA assemblies to explore the impact of salt on CA assembly. SAXS provides quantitative, solution-state data regarding the size and shape of 10−100 nm nanostructures.[28] With 50 mM NaCl and without salt, CA solutions displayed scattering slopes between −1 and −2 in the low *q* regime, indicative of 1D nanostructures with 100-nm-scale features (Figure 2a and Figure S2). The scattering from **L1** through **L7**

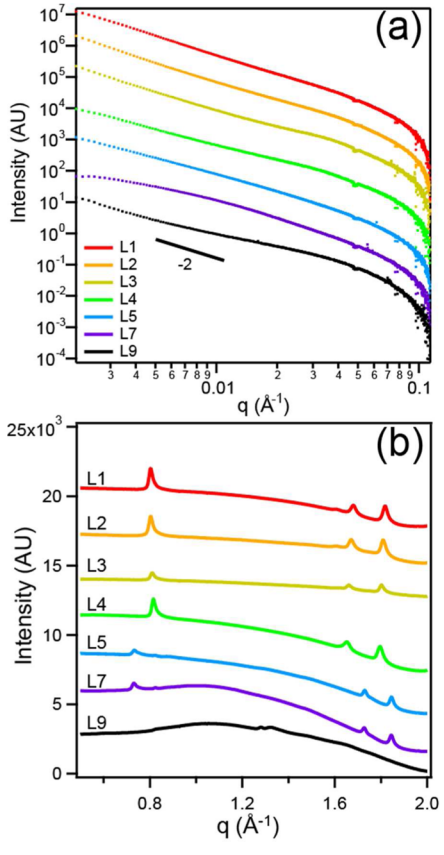

Figure 2. (a) SAXS data on CA linker series assemblies under charge-screening conditions. All samples are prepared at 9.57 mM CA and 50 mM NaCl in water. (b) WAXS data of CA linker series (9.57 mM final concentration) gelled with PDDA (0.83 wt % PDDA final concentration).

molecules was fit to a parallelepiped form factor model, approximating nanostructures as long, flat nanoribbons (Figure S3 and Table S1). Interestingly, **L9** can be modeled as thin ribbons or elliptical cylinders with diameters less than 10 nm, suggesting that this CA packs differently from others in the series.

To investigate molecular packing within nanostructures, we obtained wide-angle X-ray scattering (WAXS) data on CA

DOI: 10.1021/jacs.5b10027
J. Am. Chem. Soc. 2015, 137, 15241−15246

solutions gelled with poly(diallyl dimethylammonium chloride) (PDDA). **L1**−**L7** displayed three diffraction peaks between 0.6 and 2.0 $Å^{-1}$ (Figure 2b), a consequence of diffraction by a crystalline 2D oblique unit cell. These three peaks represent the a*, b*, and (a + b)* vectors that define the inverse-space 2D oblique lattice unit cell. Despite having identical aromatic and ionic functionalities, the unit cell dimensions differed between **L1**−**L4** and **L5**/**L7** (Table 1, Tables S2 and S3). Specifically,

Table 1. Peak Positions and Calculated Unit Cell Dimensions for CA Linker Series in Aqueous PDDA Solutions, from WAXS[a]

molecule	a (Å)	b (Å)	θ (deg)	area ($Å^2$)
L1	7.83	3.74	86.5	29.3
L2	7.83	3.77	86.5	29.4
L3	7.77	3.79	86.5	29.4
L4	7.72	3.81	86.3	29.3
L5	8.57	3.64	87.2	31.2
L7	8.61	3.64	87.3	31.3
L9	–	–	–	–

[a]See Supporting Information for determination of unit cell parameters.

the edge-to-edge chromophore distance (a vector) increases from 7.8 Å for **L1**−**L4** to 8.6 Å for **L5**/**L7** while the height (b vector), comparable to π−π stacking distances, decreases from 3.8 Å for **L1**−**L4** to 3.6 Å for **L5**/**L7**. Furthermore, many of the CAs display the same three diffraction peaks even without screening ions (Figure S4) and with NaCl instead of PDDA (Figure S5 and Table S4). The data suggest that the crystallographic unit cell dimensions are intrinsic to the supramolecular assembly in water and are not altered by the screening salt. We previously observed a similar lack of specificity to salt identity on **L5** crystalline packing,[1] suggesting that this phenomenon is a general feature of PMI CA assemblies. **L9** aqueous solutions revealed no diffraction peaks, both in unscreened and charge-screened environments, suggesting amorphous packing within these nanostructures.

The microscopy and scattering data indicate the presence of two morphologies within the CA series. Specifically, we observe a ribbon morphology (Figure 3a) capable of crystallization into two different packing arrangements for **L1**−**L7** (Figure 3b−d) and a noncrystalline 1D nanostructure with an elliptical cross section for **L9** (Figure 3e). Among the crystalline nanostructures, we observed two different unit cell patterns: a "short-linker" unit cell for **L1**−**L4** and an "intermediate-linker" unit cell for **L5** and **L7**. A similar effect, in which the imide substituent alters crystalline packing, has been observed with PDIs.[29] As **L1** has only one methylene unit, that assembly should be controlled primarily by the interplay between π−π stacking and electrostatic repulsion. As the number of methylenes is increased, we expect some additional stabilization due to increased hydrophobicity and van der Waals contacts among the molecules (up to 7 kJ/mol per methylene[30]). The observed change in crystalline packing dimensions between **L4** and **L5** could reflect a shift in the balance of noncovalent forces due to increased contribution of van der Waals attractions. An additional change from crystalline ribbons for **L7** to noncrystalline fibers for **L9** is observed, possibly resulting from frustration between the van der Waals cohesion and π−π stacking forces. Furthermore, another contribution to ordering frustration is the competition between hydrophobic interactions among the longest linkers and electrostatic repulsion of the carboxylate groups.

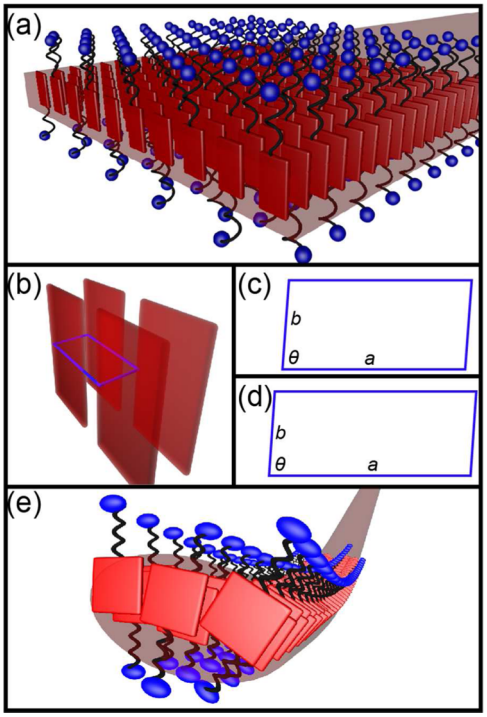

Figure 3. Representation of molecular packing within CA nanostructures. (a) Ribbon with CAs packed into 2D oblique lattice. (b) 2D unit cell with overlaid CA packing. (c) Short-linker and (d) intermediate-linker 2D unit cells with labeled parameters, scaled for comparison. (e) Proposed packing of **L9** into a cylinder with an elliptical cross section.

We were interested in determining nanostructure thickness to estimate the chromophore−catalyst distance, since this parameter should be important for the electron transfer processes during photocatalysis. We therefore investigated CA films using grazing incidence X-ray scattering (GIXS), a technique that has been previously used to elucidate CA nanostructure thicknesses by measuring the lamellar packing repeat distance in CA films.[1] These CA samples displayed diffraction peaks in the z-direction as a 1:2:3 ratio of q values with respect to the primary scattering peak, indicative of a lamellar nanostructure packing (Figure 4). Using the primary scattering peak, we found that the real-space distances increase linearly with linker length (Figure S6), except for **L9** which does not form ribbons and is therefore not expected to form a lamellar structure. The lamellar d-spacings correspond to the thickness of the ribbon-shaped nanostructures (the smallest dimension of these structures), allowing us to estimate the distance between the PMI chromophore and the external surface of the nanoscale ribbon where a catalyst molecule might bind (Table 2 and Figure S7; see Supporting Information for calculation). Although these distances appear shorter than expected based on molecular modeling, the alkyl linkers may coil or tilt relative to the nanostructure surface. Tilting between the alkyl imide substituent and aromatic perylene have been reported for other perylene imide systems[31,32] and may contribute to the off-axis scattering features that appear in **L4**−**L7** films (Figure 3d−f, white arrows and Table S5). The high propensity for these nanostructures to stack on top of one another impeded measurements of single-ribbon thicknesses by atomic force microscopy (Figure S8).

DOI: 10.1021/jacs.5b10027
J. Am. Chem. Soc. 2015, 137, 15241−15246

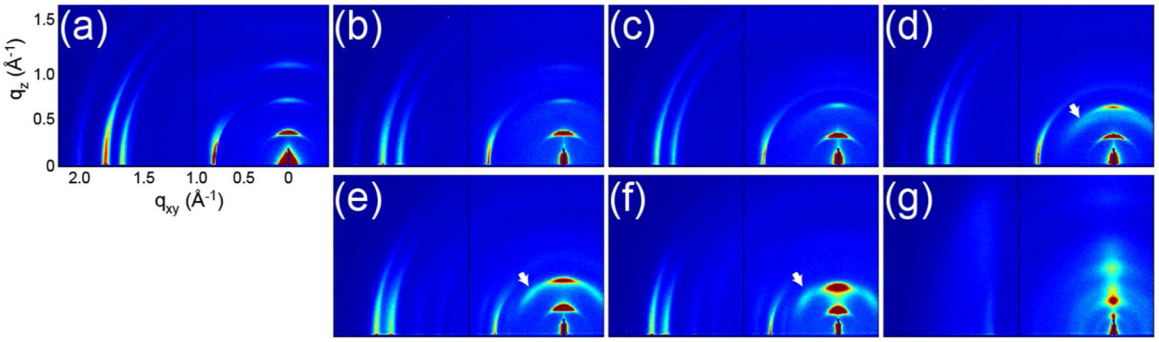

Figure 4. GIXS images collected from (a) **L1**, (b) **L2**, (c) **L3**, (d) **L4**, (e) **L5**, (f) **L7**, and (g) **L9** films on glass. Films were produced by drop-casting 100 μL of 11.5 mM CA solution onto a glass slide and allowing the solution to air-dry over several hours.

Table 2. Peak Positions and Calculated Unit Cell Dimensions for CA Linker Series in Dry Films, from GIXS[a]

	Z-axis		*XY*-plane			
molecule	thickness (Å)	PMI−Surface Distance (Å)	*a* (Å)	*b* (Å)	θ (deg)	area (Å^2)
L1	16.7	3.10	7.53	3.63	86.5	27.3
L2	17.0	3.25	7.46	3.67	85.9	27.3
L3	18.5	4.00	7.54	3.65	86.4	27.5
L4	19.0	4.25	7.41	3.63	85.9	26.8
L5	19.5	4.5	8.15	3.51	87.7	28.6
L7	21.6	5.55	8.23	3.52	87.2	28.9
L9	29.0	9.25	–	–	–	–

[a]See Supporting Information for determination of unit cell parameters.

We also observed three grazing-incidence diffraction peaks in the *xy*-plane for **L1**−**L7**, indicating that these CA assemblies remain crystalline upon drying. The unit cells of **L1**−**L7** shrink in both dimensions by 7% relative to the gel state, likely due to dehydration (Table S5). In this dry state, **L9** showed a peak corresponding to 3.7 Å, consistent with the other PMI π−π stacking distances, and a very broad feature at 4.6 Å, perhaps due to coiling or packing of the alkyl linkers. This value is comparable to interchain distances (∼4.4 Å) reported between alkyl tails within self-assembled monolayers.[33] The persistence of CA crystallinity in both hydrated and dried states could allow us to cast crystalline films for other electronic applications.

Absorbance spectra for the CA assemblies were measured in solutions that disfavor self-assembly and in the gel state under the same charge-screening conditions used in the X-ray studies. When molecularly dissolved in DMSO, **L1**−**L9** display identical absorbance patterns with a maximum at 485 nm (Figure S9), indicating that the CAs are electronically identical. This is consistent with previous reports of an orbital node at the imide nitrogen that decouples the PMI core's electron density from the imide substituent's orbitals.[34] Therefore, any differences between the assemblies must arise entirely from the local environment present within the nanostructures.

We observed in water solutions highly blue-shifted absorbance maxima for **L1**−**L7** (Figure 5), consistent with strong electronic coupling within H-aggregates arising from cofacial π−π stacking.[24] This blue shift is consistent with a decoupling of the photogenerated exciton from lattice vibrational states.[35] **L1** and **L2** displayed nearly overlapping absorbance spectra with maxima at 424 nm. In contrast, **L3** and **L4** derivatives exhibit absorbance maxima between 472 and 476, near the absorbance maxima of nonscreened assemblies (Figure S10). We also observed shoulders at 424 nm, which are

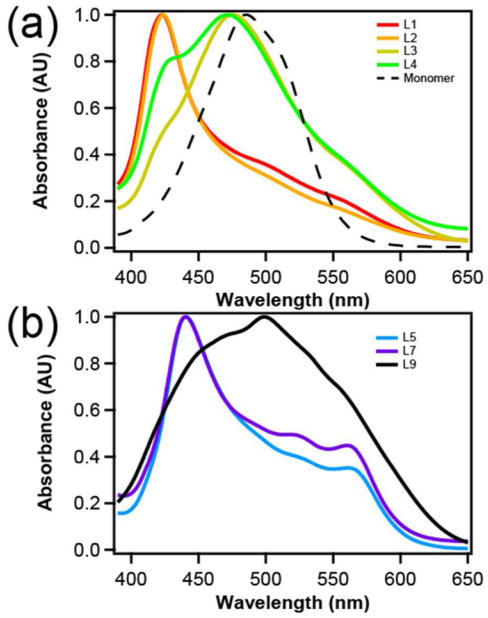

Figure 5. UV−vis absorbance spectroscopy of crystalline CAs in aqueous 50 mM NaCl. (a) Absorbance spectra of short-linker CAs. (b) Absorbance spectra of intermediate- and long-linker CAs. Salt spectra were collected at 9.57 mM CA in a 0.05 mm path length quartz cell. Monomer spectrum (shown: **L1**) was collected at 2.88 mM in 1:3 H_2O/DMSO solution in a 1 mm path length quartz cuvette.

the same as the blue-shifted maxima of **L1** and **L2** spectra. These shoulders likely represent absorbance by the crystalline assemblies observed by WAXS and GIXS. The low intensity of the shoulders suggests that many of the **L3** and **L4** molecules are not actually in a crystalline environment, possibly due to disorder within nanostructures. The **L5** and **L7** derivatives showed very similar spectra, with maxima at 440 nm, also consistent with relatively high electronic coupling among PMI moieties, although not as strongly coupled as **L1**−**L4** spectra. In contrast, **L9** showed a broad, red-shifted spectrum (with respect to the monomeric species), possibly due to translational offsets between adjacent π−π stacked PMI cores.

Interestingly, we observed an additional red-shifted peak at 570 nm for **L5** and **L7** but not **L1**−**L4**. From our proposed molecular packing, we expect all the PMI transition dipole moments to be parallel to one another, which excludes the possibility of J-aggregation commonly associated with red-shifted peaks. Similar red-shifted peaks have been previously reported for crystals of symmetric perylene diimides (PDIs) that also cannot form J-aggregates.[17] These red-shifted features

DOI: 10.1021/jacs.5b10027
J. Am. Chem. Soc. 2015, 137, 15241−15246

are a consequence of variations in HOMO−HOMO overlap among cofacially packed PDIs. The degree of in-phase orbital overlap has been found to depend strongly on the transverse and longitudinal translations between crystalline PDI molecules that appear when the imide substituent is varied.[29,36] Therefore, in our crystalline assemblies of **L5** and **L7**, the appearance of the red-shifted peak is likely due to a greater degree of in-phase HOMO−HOMO orbital overlap relative to **L1**−**L4**. This increased overlap is consistent with closer $\pi-\pi$ stacking of **L5** and **L7**, but we cannot exclude the contribution from translations of the molecular positions within the crystals. Furthermore, it has been shown that differences in orbital overlap within PDI crystals increases the crystals' abilities to create free charges upon photoexcitation, likely due to greater exciton-splitting abilities.[37] We therefore expect the observed differences in orbital overlap to alter the exciton-splitting capabilities of our crystalline assemblies formed from the various PMI molecules.

In order to explore the impact of both chromophore−catalyst distance and packing arrangements on photocatalysis, we investigated light-driven proton reduction from CA gels, similar to our previously described procedure.[1] Briefly, gels were prepared in sealed glass vessels by the addition of aqueous PDDA solutions (5 wt %) to aqueous CA solutions (11.5 mM before dilution). CA-PDDA gels were aged overnight prior to mixing with the sacrificial electron donor ascorbic acid (0.85 M, pH 4) and a water-soluble **P2N2** nickel catalyst (19.5 μM; see Figure S11 for structure). As expected, the CA gels surrounded by this highly screened solution retain the previously described molecular packing within the nanostructures (Figure S12). After 18 h of illumination, the amount of H_2 present in the headspace was measured via gas chromatography (GC). We observed that **L5** and **L7** produced significantly more H_2 than the molecules with either shorter or longer linker lengths (Figure 6).

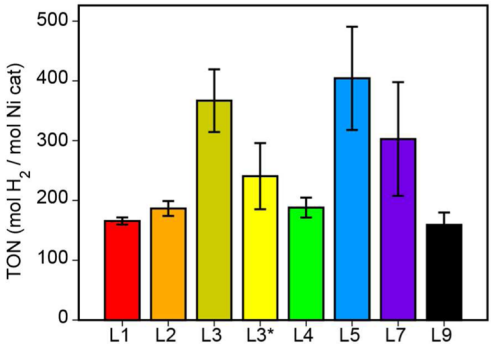

Figure 6. Photocatalytic H_2 evolution experiments of **L1** (red), **L2** (orange), **L3** (gold), centrifuged **L3** materials (L3*, yellow), **L4** (green), **L5** (blue), **L7** (purple), and **L9** (black) assemblies at 9.57 mM and 0.83 wt % PDDA. Gel-containing samples were surrounded in 0.85 M ascorbic acid/ascorbate at pH 4 and 19.5 μM water-soluble nickel catalyst. H_2 samples were purged with Ar and illuminated for 18 h prior to headspace collection.

Interestingly, we observed anomalously high H_2 photosensitization by the **L3** relative to the other short linkers (**L1**, **L2**, and **L4**). In contrast to the other CA-PDDA materials, which form gels, **L3** formed a fine red precipitate upon the addition of PDDA. SEM of the precipitate showed the precipitate to have nanostructured features similar to the other gels (Figure S13). Dilution with aqueous ascorbic acid resuspended some of this material to give an orange suspension surrounding the red solid (Figure S14). While photocatalysis with this material afforded 367 turnovers of H_2, localization of the suspension back into the precipitate via centrifugation yielded approximately 240 turnovers (Figure S15), which is more consistent with H_2 produced by **L2** and **L4** (187 and 188, respectively). It appears that the dispersed suspension can capture more of the incident light than the solid precipitate at the bottom of the tube or the other CA-PDDA gels. We observed that **L1**−**L4**, having the shortest chromophore−surface distances, yielded similar and low TONs. While short distances may favor electron transfer, charge recombination could also be favorable at these distances. Therefore, the photocatalytic activity at short distances does not appear to be dominated by the chromophore−catalyst distance. However, **L5** photosensitized more H_2 than **L7**, due to the smaller distance between the PMI core and catalyst for **L5**. Since **L4** and **L5** appear to have very similar chromophore−surface distances (see Table 2), we were surprised to observe such large differences in H_2 production. As discussed previously, **L5** and **L4** crystallize into different unit cells. This change in molecular packing of **L5** was accompanied by a red-shifted absorbance peak, indicative of relatively higher in-phase HOMO−HOMO orbital overlap within that assembly. This suggests that the two systems may adopt different pathways after absorption of a photon. We expect the mechanism of photocatalytic H_2 evolution to proceed by formation of a photogenerated exciton, followed by electron transfer from excess ascorbate in solution (330 times relative to CA and 24 000 times relative to catalyst) to give a PMI radical anion. For H_2 to be produced, the Ni catalyst must be reduced two times by CA radical anions and receive two protons from solution. Higher in-phase orbital overlaps between molecules has been shown in PDI crystals to result in higher photoconductivities.[37] It has been hypothesized that the increase in photogenerated charge carrier collection is due to increased exciton splitting efficiencies from higher orbital overlap.[36] Since **L5** has a higher orbital overlap than **L4**, it should also have a higher exciton splitting ability to generate the free charges needed for the electron transfer events required for H_2 production. Therefore, future efforts to maximize solar-to-fuel conversion would benefit from a focus on improving orbital overlaps between CA molecules.

The supramolecular assemblies formed by **L9** molecules in water, which did not reveal any crystallinity in solution, yielded the lowest values of catalytic turnovers of the homologous series studied here. While the absence of crystalline peaks makes it difficult to determine the molecular packing geometry, fluorescence measurements showed an emission maximum at 680 nm (Figure S16), comparable to known PMI excimers.[24] The low-energy excimer states formed in **L9** assemblies may function as low-energy trap states that could lower H_2 photosensitization yields. Furthermore, the **L9** chromophore−surface distance, at ∼9 Å, may also limit electron transfer to and from the aggregated PMI cores.

CONCLUSIONS

Varying the linker length connecting conjugated cores and ionizable groups in chromophore amphiphiles has very significant and not easily predictable consequences on their supramolecular structure and photocatalytic performance. Increasing the linker length results in changes to both the nanoscale morphology and molecular packing arrangements. The molecular packing for linkers of five and seven methylenes

DOI: 10.1021/jacs.5b10027
J. Am. Chem. Soc. 2015, 137, 15241−15246

showed the highest in-phase HOMO−HOMO orbital overlap, resulting in greater exciton-splitting capabilities to boost turnover numbers in photocatalytic hydrogen production. We conclude that exciton splitting within supramolecular materials for photocatalytic reactions will be critical in the development of integrated scaffolds for solar-to-fuel conversion.

■ ASSOCIATED CONTENT

Supporting Information

The Supporting Information is available free of charge on the ACS Publications website at DOI: 10.1021/jacs.5b10027.

Experimental methods, materials used, synthetic characterization, calculations, and data (PDF)

■ AUTHOR INFORMATION

Corresponding Author

*E-mail: s-stupp@northwestern.edu.

Notes

The authors declare no competing financial interest.

■ ACKNOWLEDGMENTS

This work was supported as part of the Argonne-Northwestern Solar Energy Research (ANSER) Center, an Energy Frontier Research Center funded by the U.S. Department of Energy, Office of Science, Basic Energy Sciences under Award No. DE-SC0001059. Use of the Advanced Photon Source (APS) was supported by the U.S. Department of Energy, Office of Science, Basic Energy Sciences, under Contract No. DE-AC02-06CH11357. SAXS experiments were performed at the DuPont-Northwestern-Dow Collaborative Access Team (DND-CAT) located at Sector 5 of APS. DND-CAT is supported by E.I. DuPont de Nemours & Co., The Dow Chemical Company, and Northwestern University. WAXS experiments conducted at BioCARS Sector 14 at the APS were supported by grants from the National Center for Research Resources (5P41RR007707) and the National Institute of General Medical Sciences (8P41GM103543) from the National Institutes of Health. GIXS data were collected at Sector 8-ID-E of APS. We thank the Biological Imaging Facility (BIF) at Northwestern for the use of TEM equipment and Electron Probe Instrumentation Center (EPIC) facilities of the Northwestern University Atomic and Nanoscale Characterization Experimental (NUANCE) which has received support from the MRSEC program (NSF DMR-1121262) at the Materials Research Center; the Nanoscale Science and Engineering Center (NSF EEC-0647560) at the International Institute for Nanotechnology; and the State of Illinois, through the International Institute for Nanotechnology, for the use of SEM equipment. NMR and MS equipment at the Integrated Molecular Structure Education and Research Center (IMSERC) was supported by the National Science Foundation under CHE-9871268.

■ REFERENCES

(1) Weingarten, A. S.; Kazantsev, R. V.; Palmer, L. C.; McClendon, M.; Koltonow, A. R.; Samuel, A. P. S.; Kiebala, D. J.; Wasielewski, M. R.; Stupp, S. I. *Nat. Chem.* **2014**, *6*, 964.

(2) Amunts, A.; Toporik, H.; Borovikova, A.; Nelson, N. *J. Biol. Chem.* **2010**, *285*, 3478.

(3) Lubner, C. E.; Grimme, R.; Bryant, D. A.; Golbeck, J. H. *Biochemistry* **2010**, *49*, 404.

(4) Utschig, L. M.; Silver, S. C.; Mulfort, K. L.; Tiede, D. M. *J. Am. Chem. Soc.* **2011**, *133*, 16334.

(5) Silver, S. C.; Niklas, J.; Du, P.; Poluektov, O. G.; Tiede, D. M.; Utschig, L. M. *J. Am. Chem. Soc.* **2013**, *135*, 13246.

(6) Yamamoto, Y.; Fukushima, T.; Suna, Y.; Ishii, N.; Saeki, A.; Seki, S.; Tagawa, S.; Taniguchi, M.; Kawai, T.; Aida, T. *Science* **2006**, *314*, 1761.

(7) Sofos, M.; Goldberger, J.; Stone, D. A.; Allen, J. E.; Ma, Q.; Herman, D. J.; Tsai, W.-W.; Lauhon, L. J.; Stupp, S. I. *Nat. Mater.* **2009**, *8*, 68.

(8) Loser, S.; Bruns, C. J.; Miyauchi, H.; Ortiz, R. o. P.; Facchetti, A.; Stupp, S. I.; Marks, T. J. *J. Am. Chem. Soc.* **2011**, *133*, 8142.

(9) Ruiz-Carretero, A.; Aytun, T.; Bruns, C. J.; Newcomb, C. J.; Tsai, W.-W.; Stupp, S. I. *J. Mater. Chem. A* **2013**, *1*, 11674.

(10) Aytun, T.; Barreda, L.; Ruiz-Carretero, A.; Lehrman, J. A.; Stupp, S. I. *Chem. Mater.* **2015**, *27*, 1201.

(11) Lee, O. P.; Yiu, A. T.; Beaujuge, P. M.; Woo, C. H.; Holcombe, T. W.; Millstone, J. E.; Douglas, J. D.; Chen, M. S.; Fréchet, J. M. *Adv. Mater.* **2011**, *23*, 5359.

(12) Okeyoshi, K.; Yoshida, R. *Soft Matter* **2009**, *5*, 4118.

(13) Okeyoshi, K.; Yoshida, R. *Adv. Funct. Mater.* **2010**, *20*, 708.

(14) Babu, S. S.; Praveen, V. K.; Ajayaghosh, A. *Chem. Rev.* **2014**, *114*, 1973.

(15) Wurthner, F.; Bauer, C.; Stepanenko, V.; Yagai, S. *Adv. Mater.* **2008**, *20*, 1695.

(16) Lin, H.; Camacho, R.; Tian, Y.; Kaiser, T. E.; Würthner, F.; Scheblykin, I. G. *Nano Lett.* **2010**, *10*, 620.

(17) Shahar, C.; Baram, J.; Tidhar, Y.; Weissman, H.; Cohen, S. R.; Pinkas, I.; Rybtchinski, B. *ACS Nano* **2013**, *7*, 3547.

(18) Dhar, J.; Kumar, S.; Patil, S. *J. Phys. Chem. C* **2014**, *118*, 15079.

(19) Hoeben, F. J. M.; Wolffs, M.; Zhang, J.; De Feyter, S.; Leclère, P.; Schenning, A. P. H. J.; Meijer, E. W. *J. Am. Chem. Soc.* **2007**, *129*, 9819.

(20) Hasobe, T. *Phys. Chem. Chem. Phys.* **2010**, *12*, 44.

(21) Vijayakumar, C.; Praveen, V. K.; Kartha, K. K.; Ajayaghosh, A. *Phys. Chem. Chem. Phys.* **2011**, *13*, 4942.

(22) Feiler, L.; Langhals, H.; Polborn, K. *Liebigs Ann.* **1995**, *1995*, 1229.

(23) Fuller, M. J.; Wasielewski, M. R. *J. Phys. Chem. B* **2001**, *105*, 7216.

(24) Lindquist, R. J.; Lefler, K. M.; Brown, K. E.; Dyar, S. M.; Margulies, E. A.; Young, R. M.; Wasielewski, M. R. *J. Am. Chem. Soc.* **2014**, *136*, 14912.

(25) Lefler, K. M.; Co, D. T.; Wasielewski, M. R. *J. Phys. Chem. Lett.* **2012**, *3*, 3798.

(26) Lefler, K. M.; Kim, C. H.; Wu, Y.-L.; Wasielewski, M. R. *J. Phys. Chem. Lett.* **2014**, *5*, 1608.

(27) Amara, N.; Mashiach, R.; Amar, D.; Krief, P.; Spieser, S. p. A. H.; Bottomley, M. J.; Aharoni, A.; Meijler, M. M. *J. Am. Chem. Soc.* **2009**, *131*, 10610.

(28) Cui, H.; Pashuck, E. T.; Velichko, Y. S.; Weigand, S. J.; Cheetham, A. G.; Newcomb, C. J.; Stupp, S. I. *Science* **2010**, *327*, 555.

(29) Klebe, G.; Graser, F.; Hadicke, E.; Berndt, J. *Acta Crystallogr., Sect. B: Struct. Sci.* **1989**, *45*, 69.

(30) Israelachvili, J. N. In *Intermolecular and Surface Forces*, 3rd ed.; Israelachvili, J. N., Ed.; Academic Press: San Diego, 2011; p 107.

(31) Shao, C.; Grüne, M.; Stolte, M.; Würthner, F. *Chem. - Eur. J.* **2012**, *18*, 13665.

(32) Fennel, F.; Wolter, S.; Xie, Z.; Plötz, P.-A.; Kühn, O.; Würthner, F.; Lochbrunner, S. *J. Am. Chem. Soc.* **2013**, *135*, 18722.

(33) Ulman, A. *Chem. Rev.* **1996**, *96*, 1533.

(34) Wurthner, F. *Chem. Commun.* **2004**, 1564.

(35) Spano, F. C. *Acc. Chem. Res.* **2010**, *43*, 429.

(36) Kazmaier, P. M.; Hoffmann, R. *J. Am. Chem. Soc.* **1994**, *116*, 9684.

(37) Law, K. Y. *Chem. Rev.* **1993**, *93*, 449.

DOI: 10.1021/jacs.5b10027
J. Am. Chem. Soc. 2015, 137, 15241−15246